Graphical Abstract

Flipping: a Valve-Free Strategy to Control Fluid Flow in Centrifugal Microfluidic Systems

Ali Gholizadeh*, Gabriel Mazzucchelli, Tristan Gilet

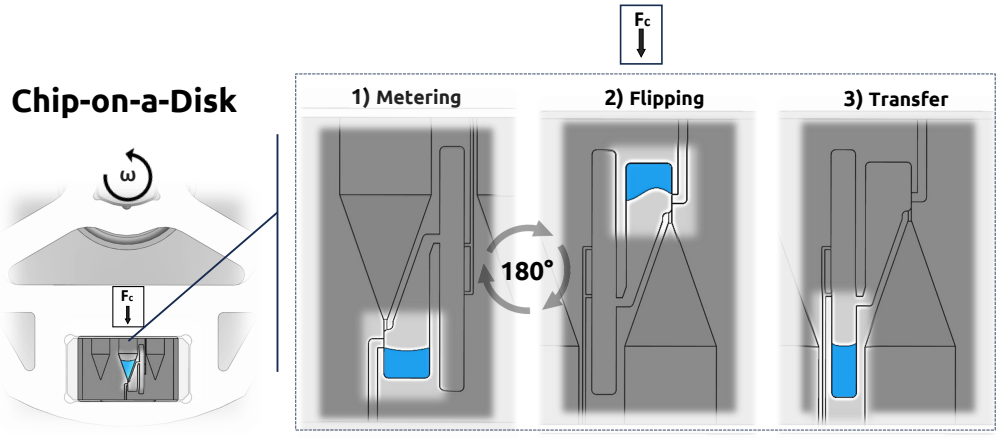

Highlights

Flipping: a Valve-Free Strategy to Control Fluid Flow in Centrifugal Microfluidic Systems

Ali Gholizadeh*, Gabriel Mazzucchelli, Tristan Gilet

- This work introduces a simple and robust valve-free strategy, here called "flipping", to control fluid flow in centrifugal microfluidic systems.
- Microfluidic chips can be repositioned on the rotating support (e.g., disk or support compatible with lab centrifuges) that enables multi-directional flow control.
- A semi-empirical physical model predicts the acceleration threshold necessary to trigger the liquid transfer.

Flipping: a Valve-Free Strategy to Control Fluid Flow in Centrifugal Microfluidic Systems

Ali Gholizadeh*[a], Gabriel Mazzucchelli[b], Tristan Gilet[a]

[a] *Department of Aerospace and Mechanical Engineering, Microfluidics Laboratory, University of Liège, , Liège, 4000, , Belgium*
[b] *Mass Spectrometry Laboratory, MolSys Research Unit and GIGA-Proteomics, University of Liège, , Liège, 4000, , Belgium*

Abstract

Centrifugal microfluidics has emerged as a technology to automate fluid handling at the microliter scale in bioassays. It has been mostly developed for point-of-care diagnostic applications, where assays involve a well-defined workflow. By contrast, this study introduces a microfluidic strategy that allows multiple workflows within the same device, thereby addressing the requirements of sample preparation steps in R&D settings. The corresponding device is a microfluidic chip that can be inserted either in a lab-on-a-disk or in the swinging-bucket of a commercial centrifuge. The control of liquid transfers from one chamber to the next is achieved by flipping the chip, thereby reorienting it in the centrifugal force field. The present experimental study describes the fluid instability that triggers the transfer upon flipping. A semi-empirical physical model is developed that predicts the acceleration threshold of the instability as a function of design parameters. By contrast to most existing control strategies in centrifugal microfluidics, the present strategy does not involve any valve. Consequently, it is robust to variations of material and sample properties, and it yields minimal fabrication constraints. Designing appropriately sized chambers enables flexible implementation of complex workflows. This strategy brings the miniaturization benefits of centrifugal microfluidics to sample preparation workflows.

Keywords: Centrifugal microfluidics, Lab-on-a-disk, Chip-on-a-disk, Bidirectional flow control, Rayleigh-Taylor instability, Sample preparation

Email address: ali.gholizadeh@uliege.be (Ali Gholizadeh*)

1. Introduction

Analytical techniques are becoming increasingly sensitive (with a very low LOQ (1)). Consequently, analyses can now be made with sample volumes in the sub-microliter range. It paves the way for applications in which the amount of material to analyze may be very limited, e.g., proteomic analyses on single cells (2), or microbiopsy in spatial omics (3). Conventional sample preparation systems work in the milliliter range, which implies extreme dilutions, and a significant risk of sample loss (4), (5). Therefore, it is necessary to reduce the scale of the sample preparation system to maintain optimal yield at each step and to avoid unnecessary dilutions.

Centrifugal microfluidics is a technology in which liquid samples with volume from nanoliters to milliliters are moved in a network of microscopic channels and chambers thanks to centrifugal forces (6), (7). The microfluidic network is commonly engraved in a disk that spins to propel fluids radially outward. Each chamber is usually associated with a unit operation on the fluids (e.g., metering, mixing, storage, filtration, separation, etc.). As no external pump is required to move the fluids, centrifugal microfluidics has emerged as a promising technique to carry out sample preparation steps in point-of-care diagnostic assays (8). The liquids move through the channels and chambers as plugs, thereby significantly reducing dead volumes when compared to lab-on-a-chip microfluidic systems (9).

Metering (also called aliquoting) is the accurate selection of a smaller and defined liquid volume from a larger liquid sample. It is a key step often present in biological assays, that is enabled at the sub-microliter scale by centrifugal microfluidics (e.g., (10), (11)). Thanks to parallelized metering, numerous samples can be processed independently on the same disk, thereby significantly reducing the time and cost of sample preparation (e.g., (10)). The metering methods can be classified into two distinct groups, namely one-stage and two-stage methods. In one-stage metering, the liquid sample remains in the metering chamber for further processing (12). Conversely, two-stage metering typically involves the use of a valve downstream of the metering chamber that opens after metering to convey the metered sample to another microfluidic chamber (11), (13).

Passive and active valves have been widely used to control fluid flow and integrate sample preparation steps. Despite their low cost, passive valves are geometry-dependent and sensitive to material properties (14), (15). There are several types of passive valves used in centrifugal systems, including cap-

illary (16) and siphon valves (17). These valves are strongly dependent on both the surface tension of the metered liquid and its contact angle with the chip materials. They usually fail for highly wetting liquids (18). Hydrophobic patches or localized surface coating may be involved in the design of capillary valves (19), although their implementation may significantly complicate the manufacturing process. Capillary valves may also either prematurely burst or remain closed longer than expected, e.g., due to manufacturing imperfections at the channel corners (20). Kinahan *et al.* (21) proposed a microfluidic strategy in which flow control is ensured through dissolvable films that are necessarily single-used. Conversely, active valves enable timely triggering for the sequential opening and closing of microchannels in response to some external stimuli. For instance, elastomeric valves can be actuated by applying some magnetic force tuned with a flyball governor system (22). Wax plugs may also serve as valves that stop fluids until they are melted (23), (24). Although effective, the incorporation of such active components in a chip increases the manufacturing complexity of the centrifugal device. It stands in contrast to biomedical diagnostic applications, where the development of low-cost devices with simple microfluidics is encouraged by both end-users and manufacturers (20), (25).

While sample preparation workflows associated with commercialized point-of-care systems are well-defined, cutting-edge biology research requires versatile and robust tools to explore, define and validate new workflows. In most studies on centrifugal microfluidics, microfluidic features are incorporated into a rotating disk, resulting in a system known as a lab-on-a-disk (LOAD). The corresponding workflow is usually unique and engraved on the disk. The small size of the disk (or other support) strongly limits the placement of all necessary flow control units in a single layer (2D architecture). Multi-layered disks (3D architecture) were introduced to circumvent this restriction, although doing so increased the cost and duration of production (26). The presence of several layers also allows non-return motion from one layer to the next (27). Furthermore, microfluidic units integrated into the disk may contain external elements such as stirrer blades (28). These components would be embedded in each disk, so they could not be reused in successive microfluidic devices. Occasionally, other rotating supports were considered, including swinging buckets (29) or lab-tubes (30). The latter supports can fit in commercial lab centrifuges that can be safely operated at high acceleration, typically up to several thousand times g.

In their simplest form, centrifugal microfluidic systems can only push flu-

ids outward, which may be a severe limitation. Several advanced strategies have been proposed to reverse the direction of liquid motion. For example, the liquid can be pushed inward by compressed air in a non-vented chamber, the compression originating from heating (31), increased centrifugation (32) or electrolysis (33). This strategy adds challenging microfluidic design constraints when it comes to achieving liquid transfer between multiple chambers at different distances from the rotating center. Another strategy consists of adding a second degree of freedom (2-DoF) to the absolute motion of the microfluidic circuit. This modification allows for reorientation of the circuit with respect to the centrifugal force. For example, the disk may comprise a bistable mechanical system in which the chip can reach two distinct orientations. The bistability is ensured, e.g., thanks to a magnet-spring system operated by the centrifugal force itself (34), or thanks to mechanical stops and a switch of position operated by the Euler force (35). Chip reorientation may also be achieved thanks to an additional servomotor placed on the disk directly below each chip (36; 37; 38; 39; 40). Such motors are usually powered through a slip ring, which increases friction and wear (a solution to this issue is to power the motors with a wireless system (41)). Finally, chip reorientation can be induced by the differential rotation of concentric shafts actuated by two distinct servomotors, either through four-link mechanisms (42) or planetary gearboxes (27). All these strategies involve dedicated centrifuge instruments (in opposition to commercial centrifuges) that comprise mechanically complex systems. These systems are prone to parasitic vibrations if not properly designed and fabricated. Moreover, the increased load on the main shaft necessarily reduces the maximum rotation speed and acceleration at which the chip may be safely rotated.

This study introduces a novel 2-DoF system for implementing sequential sample preparation steps with centrifugal microfluidics. Our manual approach simply provides bidirectional flow control with minimal instrumentation, which can be operated by non-experts in the field. This allows the manipulation of liquids at the sub-microliter scale without requesting valves. The microfluidic features (the chip) are separable from the rotating support (e.g., the disk, or a support compatible with lab centrifuges) (**Figure 1**a-b). Thanks to this separability, the microfluidic elements may be manually reoriented on-demand with respect to the direction of the centrifugal force, e.g., through flipping (Figure 1c).

In the microfluidic device described here, the dispensed liquid is centrifuged to fill a metering chamber (Figure 1c/1-2). A given volume is se-

lected, and the excess liquid is drained off. Then the microfluidic chip is flipped to pull the metered liquid into a storage chamber. During this manual flip, the direction of the centrifugal force is inverted compared to the metering step. Upon centrifugation, the liquid sample may remain stable in the initial chamber as long as the centrifugal force can be balanced by capillary forces (Figure 1c/3). When the centrifugal acceleration reaches a certain threshold, the interface of the liquid sample is destabilized and the sample flows to the next chamber (Figure 1c/4). We analyze the interface stability experimentally and provide a semi-empirical physical model to predict its threshold. We show that its behavior is robust to different liquid solvents and chip materials. This robust and versatile system may address the need for miniaturization of sample preparation steps in R&D environments.

2. Materials and methods

2.1. Design, fabrication and materials

The microfluidic chips used in the experiments were designed with SolidWorks and fabricated by the Sirris research center. They were either manufactured through PMMA milling and injection, or 3D-printed in a resin material (Detax Medicalprint, clear-04016). They were rectangular-shaped, 4.5 mm thick, 20 mm long, and 10 mm wide. Each chip comprised a central pyramidal well (two other, off-centered wells were not used for the present experiments). The well had a squared cross-section with an area of 9 mm^2 at the inlet and 0.01 mm^2 at the outlet. A microfluidic circuit including a metering and a storage chamber was engraved downstream of the well. Adhesive tape (Labelor, 3635E5-38B297) was used to cover the chips and seal the microfluidic circuits. Five different liquid solvents were considered: DI water (density $\rho \simeq 1000\ \mathrm{kg\,m^{-3}}$, surface tension $\gamma_{\mathrm{LG}} \simeq 0.072\ \mathrm{N\,m^{-1}}$), ethylene glycol (EG, Sigma Aldrich P3015, $\rho \simeq 1110\ \mathrm{kg\,m^{-3}}$, $\gamma_{\mathrm{LG}} \simeq 0.045\ \mathrm{N\,m^{-1}}$), a water-glycerol mixture (Sigma Aldrich G5516, 50%-50% by volume, $\rho \simeq 1140\ \mathrm{kg\,m^{-3}}$, $\gamma_{\mathrm{LG}} \simeq 0.068\ \mathrm{N\,m^{-1}}$), an aqueous solution of sodium dodecyl sulfate (SDS 0.1% or 3.5 mM, Sigma Aldrich 74255, $\rho \simeq 1010\ \mathrm{kg\,m^{-3}}$, $\gamma_{\mathrm{LG}} \simeq 0.052\ \mathrm{N\,m^{-1}}$), and phosphate-buffered saline (PBS, Lonza 17-512F, $\rho \simeq 1000\ \mathrm{kg\,m^{-3}}$, $\gamma_{\mathrm{LG}} \simeq 0.061\ \mathrm{N\,m^{-1}}$). The surface tension of SDS and PBS solutions was measured with the pendant drop technique. The advancing and receding contact angles, denoted θ_{a} and θ_{r} respectively and associated with each pair of liquid vs. chip material, were measured optically. They are given in **Table 1**.

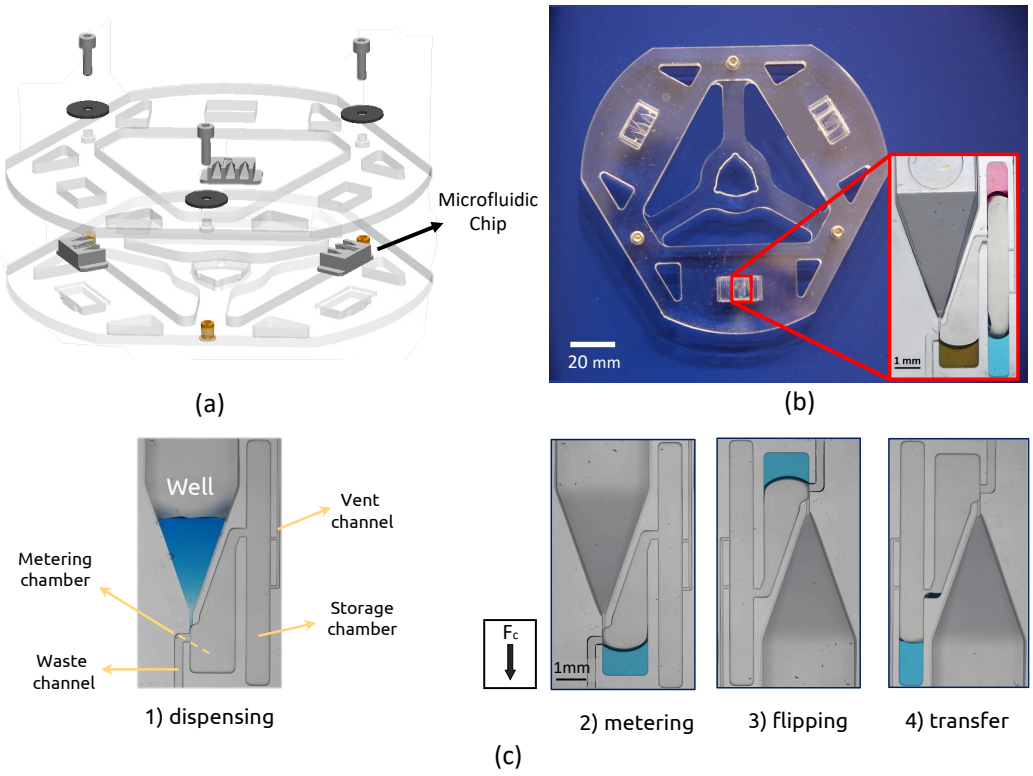

Figure 1: (a-b) Three microfluidic chips were sandwiched between two PMMA layers, thereby forming a disk that could be centrifuged. (a) Exploded CAD view. (b) Actual device. The inset is a zoom on the microfluidic features of a chip. Diluted dye solutions were metered, stored in different chambers, and prepared for mixing, through a sequence of centrifugation and flipping steps described in the next sections. (c) Microscope views of the chip after each step of a typical sequence. The chip contains an inlet well, a metering chamber, and a storage chamber. 1) 5 µL of diluted blue dye (sample) were initially dispensed in the well. 2) Upon centrifugation at 56 g, the sample moved into the metering chamber that selected 720 nL (the remainder flew to the waste). 3) The chip was detached from its support, flipped, and reattached. 4) Upon centrifugation at 110 g, the sample was transferred to the storage chamber. A scale bar is visible in c2, the scale is the same in (c1-c4).

Table 1: Measured advancing and receding contact angles (θ_a, θ_r) of the different pairs of liquid and chip material considered in these experiments.

Solution (Material)	$\theta_a[^\circ]$	$\theta_r[^\circ]$
Water (Tape)	102	72
EG (Tape)	97	60
Glycerin 50% (Tape)	99	68
SDS 0.1% (Tape)	89	49
PBS (Tape)	106	71
Water (PMMA)	91	64
EG (PMMA)	64	42
Water (Resin)	89	57
Glycerin 50% (Resin)	76	55
SDS 0.1% (Resin)	73	40
PBS (Resin)	89	62

2.2. Experimental setup

The microfluidic chips were specifically designed to enable centrifugation in two configurations with different rotating supports, motors, and instrumentation. In the first configuration, referred to as chip-on-a-disk, three microfluidic chips were sandwiched between two disk-shaped PMMA layers screwed together (Figure 1a). The chips were positioned 5 cm from the center of the resulting disk, and equidistant from each other. This unified structure mimics LOAD platforms while providing greater flexibility by allowing the use of different materials and microfluidic designs on the same disk. As a result, the manufacturing time and cost of the prototypes were drastically reduced. A centrifugal bench was built to control the disk rotation. The angular speed could go up to 3000 rpm, which corresponded to a centrifugal acceleration of 504 g at the radial position of the microfluidic chambers (**Figure 2**a). The setup comprised a computer-controlled stepper motor associated with a vertical shaft on which the disk was placed. A high-speed camera, either a Photron AX50 camera for monochromatic (grayscale) imaging or a Phantom MIRO M110 camera for color imaging, was used with a macro lens (Zeiss Milvus 2/100M) to image the chips from the top. The motor controller sent a trigger signal to the camera once per rotation to image the region of interest (ROI). The motion blur in the tangential direction was reduced to 10 µm thanks to an exposure time of 11 µs. The resolution was 10 µm pixel^{-1}. In the second configuration, referred to as chip-off-a-disk, we simply placed the microfluidic chips in a conventional lab centrifuge (Ep-

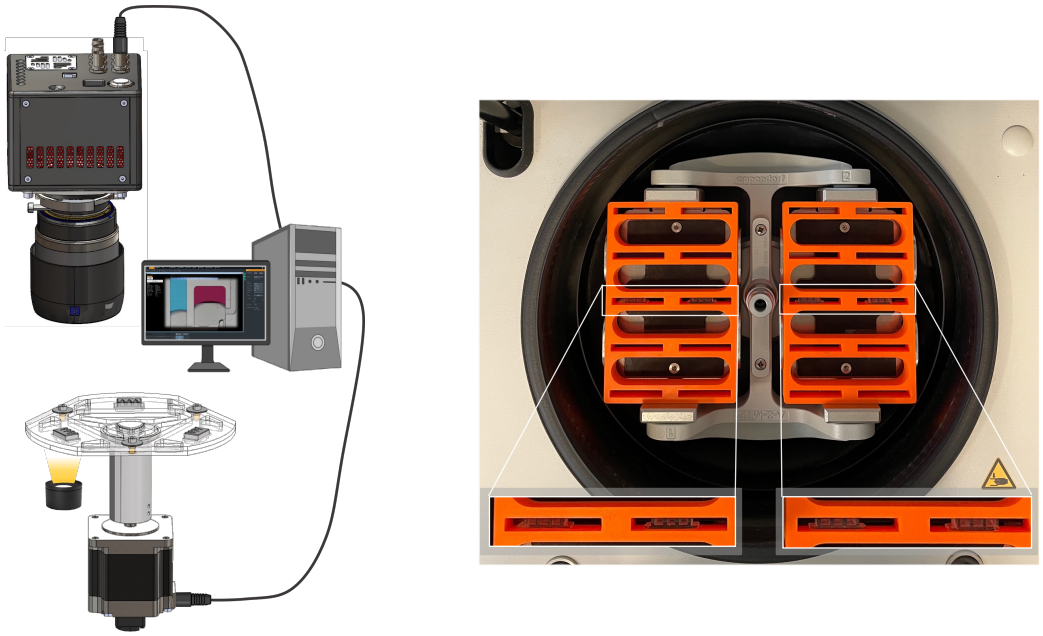

Figure 2: Microfluidic chips were centrifuged in two configurations: (a) Chip-on-a-disk: a homemade centrifugal setup was used to centrifuge the disk at different speeds up to 3000 rpm (chip at 504 g). A camera was triggered once per rotation to image the microfluidic chip. (b) Chip-off-a-disk: Four chips were placed vertically within a 3D-printed support that fitted into the swinging-bucket rotor of a commercial lab centrifuge. The centrifuge could spin at up to 4680 rpm (chip at 2204 g).

pendorf 5430R) thanks to 3D-printed supports adapted to a swinging-bucket rotor (A-2-MTP) (Figure 2b). This centrifuge machine enabled rotation at a maximum speed of 4680 rpm, which corresponded to 2204 g within the bucket. In the centrifuge machine, the motion of the fluids within the chip could not be imaged in real-time. Instead, once centrifugation was stopped, the microfluidic chip was removed from its support and transferred for observation in bright field microscopy (Zoom Advanced 2, with camera Canon EOS 5D mark III). The resolution was 0.5 µm pixel^{-1}.

2.3. Chip preparation and testing

The microfluidic chips were cleaned with isopropanol (VWRC20922-364) both after fabrication and after each set of experiments. Chips were then dried with compressed air and sealed with adhesive tape. For each experiment, we first dispensed 5 µL of liquid in the well and centrifuged to meter a sub-microliter volume. Then the microfluidic chip was flipped in order to transfer the metered liquid into the storage chamber by reversing the direction of the centrifugal force. Once the liquid was in the storage chamber, the chip was flipped a second time and an attempt at transferring the liquid to the other side of the storage chamber was made. We considered 15 metering chambers and 9 storage chambers, with similar qualitative shapes but different sizes. The width of the metering (resp. storage) chamber varied from 0.4 mm to 3 mm (resp. from 0.45 mm to 1.6 mm), while its depth varied from 0.2 mm to 1.6 mm (resp. from 0.1 mm to 1.2 mm). The liquid volume selected in the metering (resp. storage) chambers varied from 24 nL to 3.2 µL (resp. from 150 nL to 3.2 µL). The instability threshold was defined as the centrifugal acceleration beyond which the liquid was transferred from one chamber (or side) to the opposite chamber (or side). In the chip-on-a-disk configuration, it was measured by imaging the liquid motion in real-time, while incrementing the angular speed from 900 rpm (45 g) to 3000 rpm (504 g) with increments of 20 rpm every 5 seconds. At each increment, the angular speed was increased at 1000 rpm s^{-1}, so the transition lasted approximately 20 ms. The rotation was stopped as soon as the transfer of liquid was observed. In the chip-off-a-disk configuration, the flipped chips were centrifuged for 30 s at constant angular speed, then removed from the centrifuge and the possible occurrence of the instability was deduced from microscope observation. These steps were repeated with an acceleration increased from 200 g to 1300 g by steps of 100 g.

2.4. Data Analysis

The instability threshold was measured for metering and storage chambers of different sizes with water in PMMA chips. Additional measurements were made for some configurations with other liquids, and/or resin chips instead of PMMA chips. Measurements were made with the chip-on-a-disk setup, except for the configurations yielding very high thresholds that could only be tested with the chip-off-a-disk setup. At least four independent threshold measurements were taken for each considered configuration (chamber, liquid, chip material). The data analysis and model fitting are solely based on the median of these measurements for each configuration.

3. Results

3.1. Phenomenology

3.1.1. Metering

The time sequence of the metering process is illustrated in **Figure 3**. A volume of 5 µL of blue-dyed water was dispensed into the well. The chip was then centrifuged at 14 g to initiate the fluid motion. The centrifugal force was then increased to 56 g, and the liquid was compelled to ingress the metering chamber while the excess liquid was efficiently drained through the waste channel. The metering step was achieved in one second. It successfully selected a certain amount of liquid within the metering chamber. If necessary, the chips were centrifuged again at 504 g to perfectly empty the waste channel. The selected volume in the metering chamber was measured ($\pm 5\%$) with the image processing software ImageJ.

3.1.2. Instability upon "flipping"

The time sequence of the instability generated after having flipped the chip is shown in **Figure 4**. Flipping and centrifuging the microfluidic chip allowed the liquid sample to move out of the metering chamber. Before any rotational motion was applied, the interface was in a stable equilibrium state. Upon rotation at a given acceleration (110 g in Figure 4), a gradual destabilization of the interface was observed. Systematically, the contact line on the opposite side to the waste channel advanced, while the contact line at the entrance of the waste channel remained pinned. In figure 4, the thickness of the line delimiting the liquid/air interface provides information on the direction of motion of the contact line on both faces parallel to the plane of view

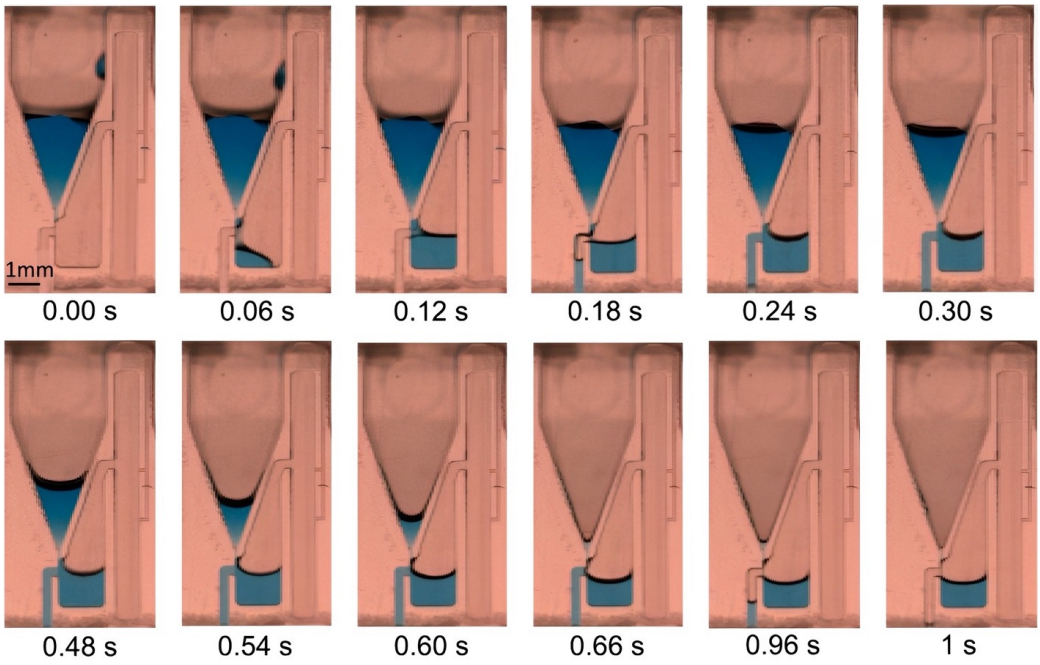

Figure 3: Snapshots were taken during the metering step. After having dispensed 5 µL of blue-dyed water in the well, the chip was centrifuged at 56 g. The liquid first invaded the metering chamber (width $W = 1.5$ mm, depth $H = 0.5$ mm), then the waste outlet (bottom left). Centrifugal forces progressively pushed the liquid through the waste outlet (depth 0.3 mm). The liquid in the metering chamber ($\simeq 720$ nL) separated from the liquid in the waste outlet. The acceleration was finally increased to 504 g to remove the liquid plug in the waste channel.

(a smaller local contact angle results in a larger interface curvature and subsequently in a wider zone of total reflection of light across the interface). The thicker line at the center of the chamber corresponds to a receding contact line, while the thinner line on the wall opposite to the waste corresponds to an advancing contact line. The liquid was progressively transferred out of the metering chamber by creeping on the sealing tape and the opposite wall to the waste channel. It took less than a second for the liquid to fully reach the storage chamber. The left/right asymmetric design of the metering chamber played a key role in dictating the direction of the liquid interface. Some liquid remained a fraction of a second longer on the side of the waste channel. It was quickly pulled down, without having the opportunity to penetrate the narrow channel leading back to the well. A similar instability was observed when the liquid plug was in the storage chamber (**Figure 5a**). Centrifuging the chip at 162 g was proved sufficient to initiate the interface destabilization. Subsequently, the liquid was entirely moved downward in less than 40 ms (t = 3.03 s). The symmetric design of the storage chamber allowed the contact line to move without any imposed direction. In particular, the liquid was seen to creep significantly along the tape during the instability.

3.1.3. Combination of unit operations

The flipping strategy allowed us to independently handle liquids in chambers of different sizes with different acceleration thresholds. This also enables controlling the movement and storage of different liquids within a microfluidic device. **Figure 6** illustrates the key steps and outcomes of this strategy in a centrifugal microfluidic device manipulating three selected volumes of different dye solutions without mixing. In the initial step, an aqueous solution of blue dye dispensed in the inlet well was metered thanks to centrifugation at 56 g. The selected volume was about 730 nL, in a chamber of width W = 1.5 mm and height H = 0.5 mm. The other chambers remained empty. Subsequently, the device was flipped and centrifuged at 110 g, which induced the transfer of the metered blue sample into the storage chamber of width W = 0.8 mm and height H = 0.5 mm (Figure 6a). The device was flipped again, and another aqueous solution of red dye was metered through centrifugation at 56 g. The selected volume was measured to be about 710 nL. So far, this gentle acceleration was insufficient to dislodge the blue sample from the storage chamber (Figure 6b). To separately isolate red and blue samples in the storage chamber, the acceleration was increased to 162 g, which moved the blue sample towards the other side of the storage chamber (Figure 6c).

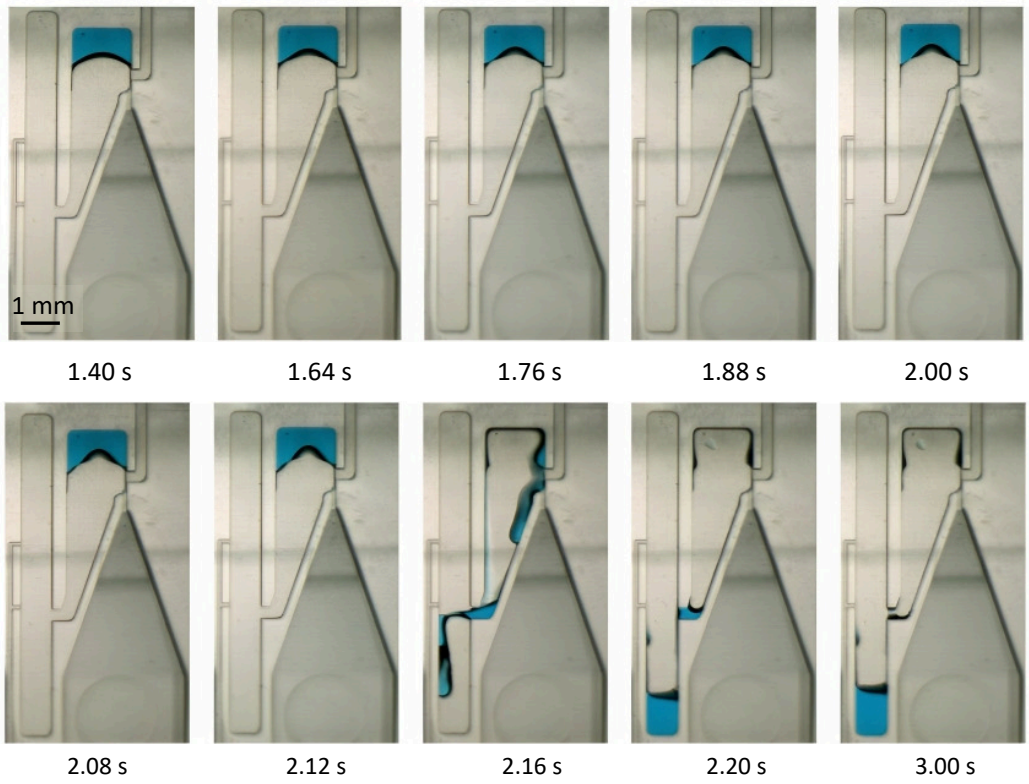

Figure 4: Time sequence illustrating the destabilization of the liquid interface in the metering chamber (width $W = 1.5$ mm, depth $H = 0.5$ mm) when the chip was flipped and then centrifuged again. Before rotation, the interface was in static equilibrium. The rotation speed was ramped from rest to 1400 rpm (110 g) at 1000 rpm s^{-1}, so the final speed was reached after 1.40 s. At 110 g, the interface was destabilized in less than 1 s. Owing to the left/right asymmetry of the chamber induced by the presence of the waste outlet channel (top right), the liquid interface moved downward on the left side. A tiny volume of liquid remained a fraction of a second longer on the right side of the chamber, before being pulled down. The liquid could not penetrate the narrow channel (0.1 mm) that led back to the well. In a fraction of a second, the liquid was entirely transferred to the storage chamber.

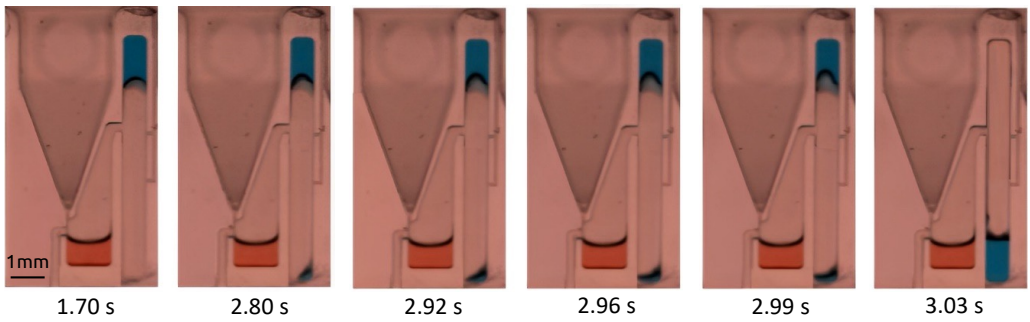

Figure 5: Time sequence illustrating the destabilization of the liquid interface in the storage chamber (width $W = 0.8$ mm, depth $H = 0.5$ mm) when the chip was flipped and then centrifuged again. Before rotation, the interface was in static equilibrium. The rotation speed was ramped from rest to 1700 rpm (162 g) at 1000 rpm s^{-1}, so the final speed was reached after 1.70 s. Owing to the symmetric design of the storage chamber, the liquid interface moved downward either along the tape or the chamber walls.

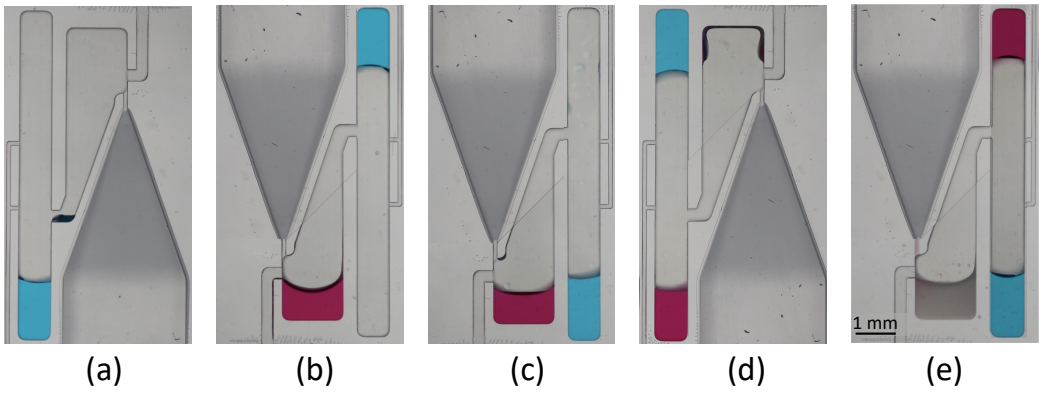

Figure 6: Liquid samples in chambers with different sizes (and consequently different acceleration thresholds) can be handled independently. Metering chamber: width $W = 1.5$ mm and depth $H = 0.5$ mm. Storage chamber: width $W = 0.8$ mm and depth $H = 0.5$ mm. (a) A given volume of blue dye sample was transferred to the storage chamber after being metered. (b) Upon centrifugation at low acceleration (i.e., 56 g), a second, red dye sample was metered. However, the acceleration was not sufficient to dislodge the blue sample from the storage chamber. (c) Increasing the acceleration above the threshold (162 g) pulled the blue sample towards the other side of the storage chamber. (d) The red sample was transferred to the storage chamber at 110 g; the blue and red samples were not merged. (e) A third sample containing a gray dye sample was metered while the red sample remained in position.

Upon flipping, the red sample was then transferred to the storage chamber at 110 g. At this stage, the blue and red samples were still kept separated, one on each side of the storage chamber (Figure 6d). Finally, a third solution was dispensed in the inlet well and pushed to the metering chamber upon centrifugation at 56 g (Figure 6e). Although the storage chamber had already been wetted by both red and blue samples, the red sample remained at its attributed location in the storage chamber. This exemplary workflow demonstrates the ability of the technique to independently manipulate individual liquid samples sequentially loaded in the device thanks to well-chosen levels of acceleration. Merging the different samples in the storage chamber would have been possible too, by choosing a different sequence of accelerations.

3.2. Instability threshold

We measured the instability acceleration threshold associated with each configuration (various metering and storage chambers, liquids and chip materials). The variation of this threshold with chamber width (for a given depth $H = 0.2$ mm) is shown in **Figure 7**. The threshold decreases with an increase in width. It is also systematically smaller for EG than for DI water. A careful look at the complete set of measurements (cf. table available in supplementary material) reveals that the threshold also decreases with increasing depth, though the variation is significantly less pronounced than the dependence on chamber width. Interestingly, the threshold remains relatively constant when only the volume of liquid in a given chamber is varied (cf. metering chamber with $W = 1.5$ mm and $H = 1$ mm, and storage chamber with $W = 0.8$ mm and $H = 0.5$ mm, in the data table in the supplementary material).

Assuming negligible contact angle hysteresis and a contact angle close to 90°, the dependence of the acceleration threshold (a_c) on chamber dimensions and liquid properties can be estimated from an energy analysis developed in the appendix. This analysis suggests that the interface remains stable when

$$a < a_c = \frac{\gamma_{LG}}{\rho}\left(\frac{c_1}{W^2}\right) + \frac{\gamma_{LG}}{\rho}\left(\frac{c_2}{WH}\right) + \frac{\gamma_{LG}}{\rho}\left(\frac{c_3}{H^2}\right), \tag{1}$$

where γ_{LG} and ρ are the liquid surface tension and density, respectively. Dimensionless coefficients c_1, c_2 and c_3 are explicitly dependent on the slope of the liquid-air interface (A.13). Subsequently, they depend on the contact angle at each wall. They may also likely depend on contact angle hysteresis, which has been neglected in the analysis. These coefficients are determined by

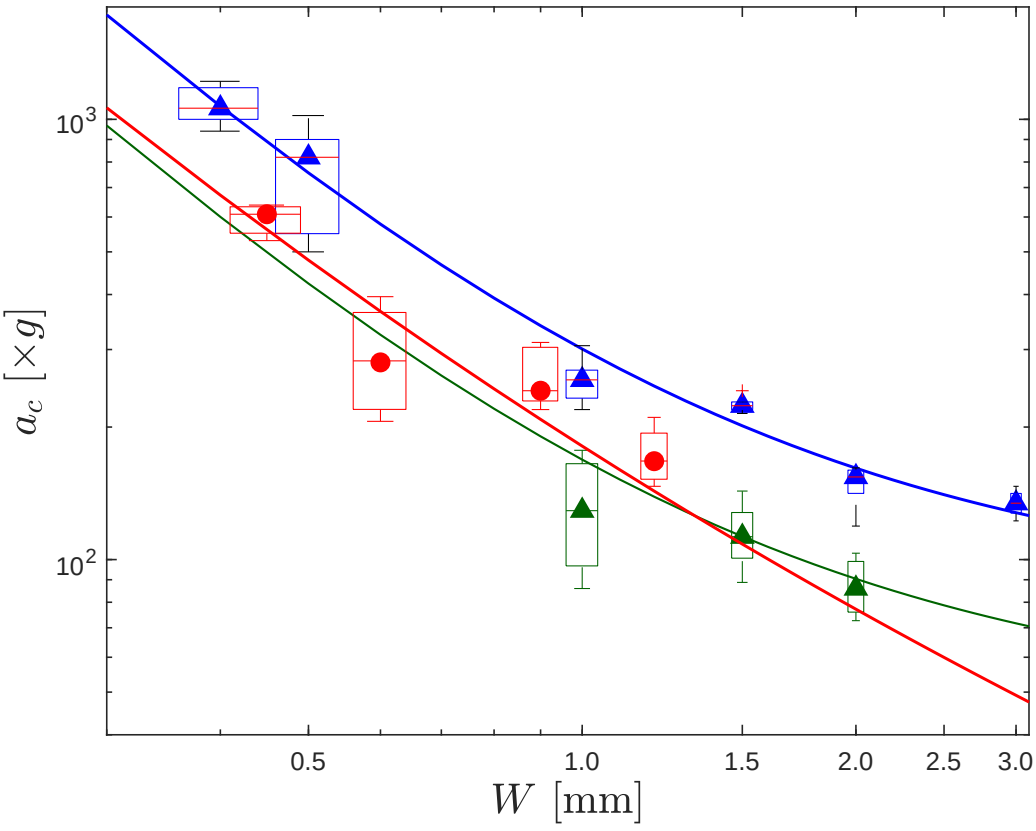

Figure 7: Threshold acceleration a_c (in g) as a function of chamber width W (in mm), for chambers of same depth $H = 0.2$ mm, in PMMA chips. The box plots represent the threshold measurements (median, quartiles and whiskers of the distribution of measured values). The solid lines represent the prediction from Equation (1). Blue symbols and curve correspond to water in metering chambers; red symbols and curve correspond to water in storage chambers; and green symbols and curve correspond to EG in metering chambers.

the linear regression of **Equation (1)** on the measured acceleration threshold (median of measured values for each configuration). Although the coefficients are expected to be independent of W and H, they may still depend on the exact shape of the interface in equilibrium, the wetting properties of the solid walls, and the boundary conditions that the liquid-air interface is subjected to. For this reason, different sets of coefficients were determined for the metering and the storage chamber. Only the data obtained with water on PMMA chips were used for this linear regression. The coefficients that minimize the residual on threshold acceleration are $c_1 = 15.97$, $c_2 = 2.82$ and $c_3 = 0.44$ for the metering chamber (fit on 15 data points), and $c_1 = 8.17$, $c_2 = 3.21$ and $c_3 = 0.017$ for the storage chamber (fit on 9 data points). The threshold values predicted by Equation (1) with these coefficients for each configuration are compared to the measured values in the parity plot of **Figure 8**. The agreement is very good, with a coefficient of determination $R^2 = 0.99$ for the metering chambers, and $R^2 = 0.95$ for the storage chambers. Remarkably, the coefficients adjusted to water/PMMA data predict the instability threshold of every other considered fluid/solid configurations (EG/PMMA, water/resin, glycerin 50%/resin, and PBS/resin) with reasonable accuracy, typically within ±15%. This is likely due to the fairly similar contact angles across these configurations. However, for SDS 0.1%, which corresponds to the smallest contact angles, there is an overestimation by a factor of 1.32. This factor was determined by taking the median of the calculated ratio $a_c^{(\text{model})}/a_c^{(\text{measured})}$ across three sets of dimensions considered for the metering chamber of resin chips.

4. Discussion

The observed phenomena are reminiscent of a Rayleigh-Taylor instability, in which the centrifugal (inertial) forces destabilize the liquid interface, while capillary forces stabilize it. A few previous studies investigated this instability for liquids confined in a rectangular chamber, and only with ideal boundary conditions (e.g., Weislogel & Hsieh (43), Jacobs & Catton (44)). The proposed equation also captures this balance of centrifugal and capillary forces. By adjusting coefficients, one could make this equation valid for other, arbitrarily complex boundary conditions. Such cases would be hard to simulate numerically and there would be no hope of a closed-form *ab initio* description of the fluid instability, especially in the presence of significant contact angle hysteresis. Therefore, the present equation with adjustable co-

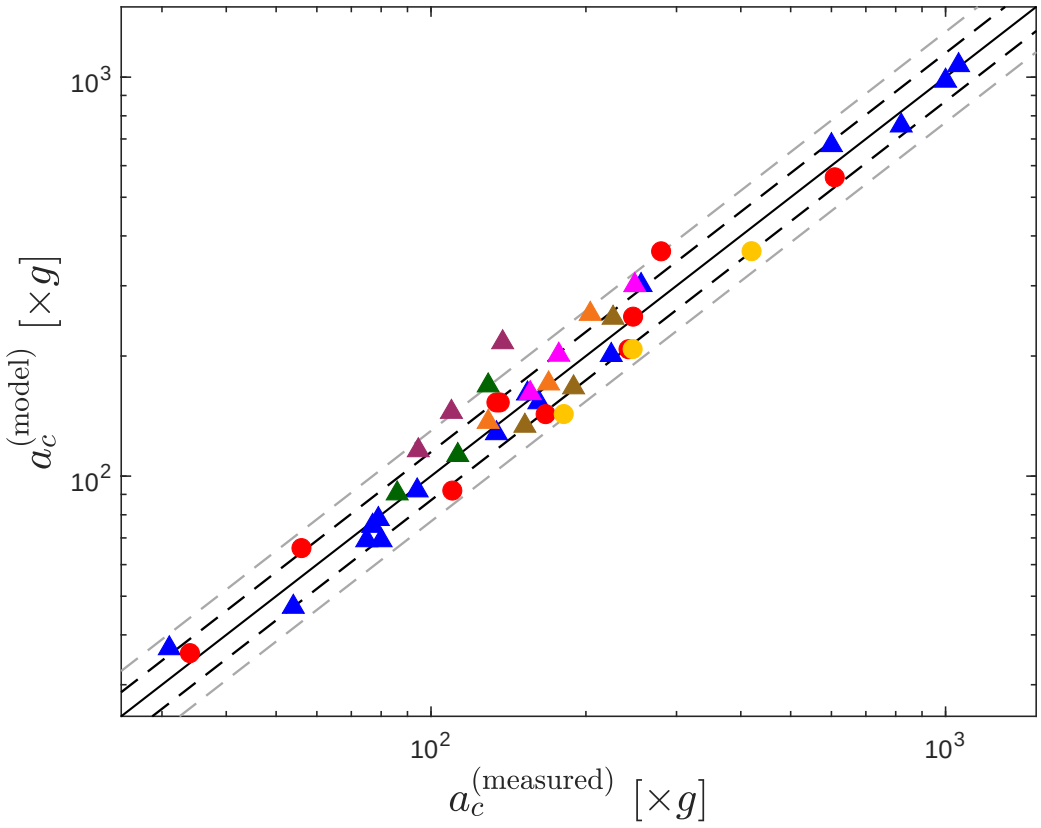

Figure 8: Parity plot comparing the threshold acceleration measurements to the predictions from Equation (1), with coefficients given in the main text obtained with water in metering and storage chambers on PMMA chips. The coefficient of determination for water - PMMA data is $R^2 = 0.99$ (resp. $R^2 = 0.95$) for the metering (resp. storage) chamber. Different symbols and colors correspond to different configurations: (Blue triangles) water – metering – PMMA, (Magenta triangles) water – metering – resin, (Green triangles) EG – metering – PMMA, (Purple triangles) SDS 0.1% – metering – resin, (Brown triangles) Glycerin 50% – metering – resin, (Orange triangles) PBS – metering – resin, (Red circles) water – storage – PMMA, and (yellow circles) water – storage – resin. Black and gray dash lines indicate discrepancies of ±15% and ±30%, respectively.

efficients represents the best option to quickly estimate the threshold when designing similar microfluidic systems. The fact that the adjusted coefficients are of order unity confirms the validity of the model. Moreover, measurements obtained with a variety of liquids on another chip material (i.e., resin) can be predicted very well with coefficients adjusted for DI water on PMMA chips. For example, as the ratio $\gamma_{\mathrm{LG}}/\rho$ of EG is almost half that of water, the good prediction indicates that the dependence of the threshold on $\gamma_{\mathrm{LG}}/\rho$ is correctly captured by Equation (1). As observed experimentally (Figure 7), the primary factor affecting the instability threshold is the chamber size, and more specifically the width W and depth H, at the level of the liquid interface. A smaller chamber yields an increased energy cost per unit volume to modify the curvature of the liquid interface, and consequently a higher acceleration threshold. For given W and H, there is no significant dependence on liquid volume: only the position of the liquid interface matters, and the amount of liquid above does not.

Furthermore, our experimental results reveal that the boundary conditions imposed on the interface by the microfluidic design have an impact on the instability threshold. The contact line is free to move in the storage chamber (actually, its motion is still limited by contact angle hysteresis), while it is partially pinned at the entrance of the waste channel in the metering chamber. This pinning condition constrains the interface deformation and consequently stabilizes its shape, which yields a higher threshold than for a storage chamber of similar dimensions (Figure 7).

While the adjusted coefficients always satisfy $c_1 \gg c_2 \gg c_3$, the corresponding terms in Equation (1) may still be of the same order of magnitude since $W > H$. In **Figure 9**, the ratios of second to first term $[c_2 W/(c_1 H)]$ and third to first term $[c_3 W^2/(c_1 H^2)]$ of Equation (1) are plotted against the effective capillary length $\lambda = \sqrt{\gamma_{\mathrm{LG}}/(\rho a_{\mathrm{c}})}$. For the metering chamber, the term in c_1/W^2 clearly dominates both other terms of Equation (1), as long as $\lambda < H$. The primary dependence of the threshold on W is expected when $W > H$, since a perturbation of the interface in the x-direction generates less curvature (and therefore less interfacial energy, so it is more unstable) than a perturbation of similar amplitude in the y-direction. This is observed at time 2.12 s in Figure 4 (the perturbation is in the left-right direction, not in the front-back direction). Nevertheless, when $\lambda > H$, the threshold exhibits a significant dependence on H. This can be explained as follows. The height of a static liquid meniscus scales as the capillary length (45), and so should the maximum difference of elevation between two points of the interface at

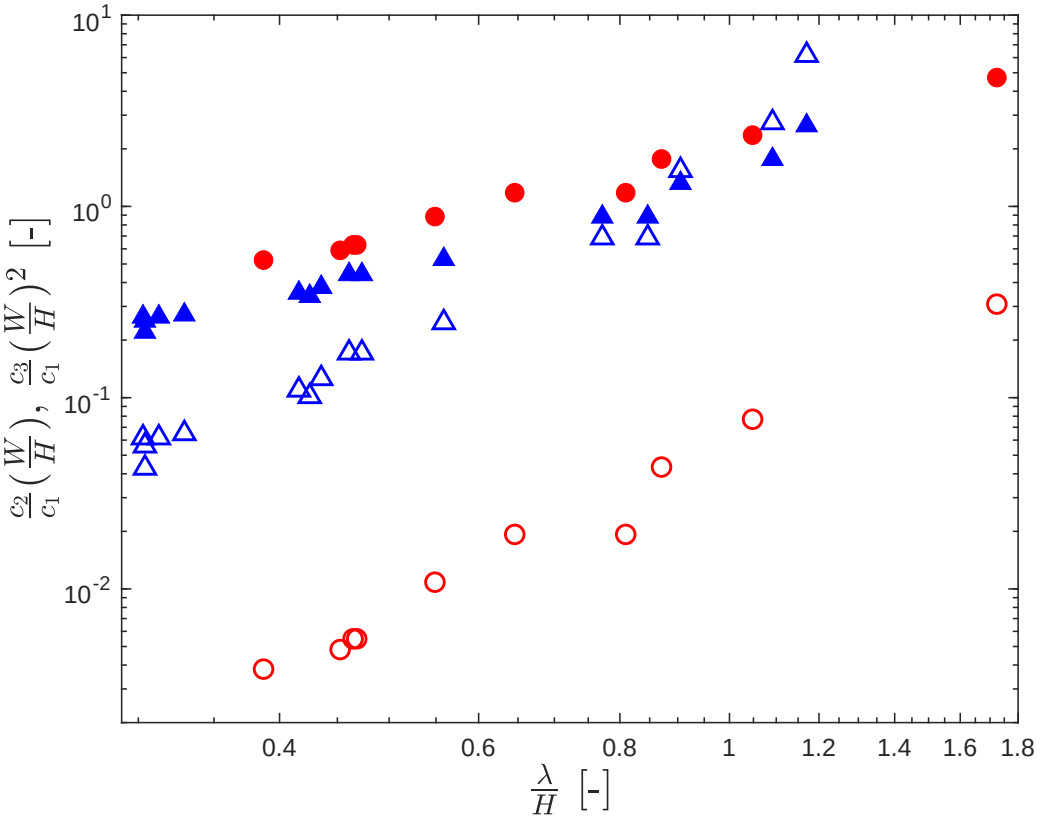

Figure 9: Variation of acceleration ratios $\frac{c_2}{c_1}(W/H)$ (filled symbols) and $\frac{c_3}{c_1}(W/H)^2$ (empty symbols), with the ratio of capillary length and depth. Blue triangles (resp. red circles) correspond to water in the metering (resp. storage) chamber on PMMA chips.

equilibrium. Consequently, the interface inclination with respect to the plane normal to centrifugal force is of the order of λ/H. When $\lambda/H > 1$, the interface is significantly inclined in both directions. The corresponding term $\partial_x f\, \partial_y f\, \partial_{\tilde{x}}\eta\, \partial_{\tilde{y}}\eta$ in **Equation (A.13)** becomes significant, and so is the corresponding term $c_2/(WH)$ in Equation (1). The same trend is observed for the storage chamber, although the term in $c_2/(WH)$ is never negligible. This is in agreement with the observation that the interface is often inclined in the storage chamber (Figure 5), with some significant differences in elevation between the tape wall and the opposite chip wall. From an engineering point of view, the table in Supplementary Material confirms that the terms involving H bring a negligible contribution to the threshold as long as $1 < W/H < 3$. For larger aspect ratios, these H terms have to be taken into account.

Our analysis of the instability threshold seems robust to variations in liquid and chip material properties. Nevertheless, the contact angles were not strongly varied in these experiments, and we still expect some variation of the model coefficients with both advancing and receding contact angles. This is particularly evident in the case of SDS 0.1%, where the receding contact angle is much smaller than for other solvents. As a result, the instability threshold for SDS 0.1% in the metering chamber of the resin chip was overestimated by a factor of 1.32. Although less roughness is expected on the surface of horizontal walls in a resin chip, the printed layers can form vertical walls in a microchannel/chamber with higher roughness than the machined microchannels/chambers on PMMA. An attempt was made to highlight the influence of surface roughness and any varying parameters between resin and PMMA chip while using the same liquid (water) in the experiments. As a result, we observed an overestimation (resp. underestimation) of the instability threshold by a factor of 1.14 (resp. 0.84) for the metering (resp. storage) chamber. Moreover, we checked that the microfluidic system does not work with perfectly wetting liquids (e.g., most oils on PMMA, or highly-concentrated SDS solutions on resin) that wick the entire microfluidic network upon initial filling of the inlet well.

5. Conclusions

This study investigated a microfluidic system in which fluids were moved controllably thanks to the reorientation (flipping) of microfluidic chips in a centrifugal force field. While this flipping is not possible with the monolithic disks found in most lab-on-disk systems, we achieved it by decoupling the

microfluidic chips from their rotating support (either a disk or the swinging bucket of a centrifuge): the chips were simply clamped on the support and could be flipped between successive centrifugation runs. Clamping the chips also proved to be an efficient and cost-effective approach for testing and developing microfluidic designs. The fluid trapped at the bottom of microfluidic chambers moves away upon flipping if the centrifugal acceleration is higher than a given threshold. This fluid instability is analogous to Rayleigh-Taylor instability. We measured this threshold for various chamber geometries and dimensions, fluids, and chip materials. We proposed a semi-empirical physical model with three coefficients adjusted to capture the threshold dependence on these parameters. The instability threshold was found to be primarily influenced by the chamber dimensions (width W and depth H) at the level of the liquid-air interface. Smaller dimensions yield a higher threshold. The relative influence of W and H was discussed and correlated to the shape taken by the interface at equilibrium, which is dictated by the effective capillary length λ. This instability threshold is a key parameter for the design of complex microfluidic workflows based on the flipping/reorientation strategy. Chambers with different functions may have different sizes, so liquids therein would only be dislodged when their respective threshold is reached. It is therefore possible, at intermediate accelerations, to dislodge fluids only in the largest chambers and not in the others. This allows the temporary storage of different fluid samples in different chambers, and their merging/mixing on demand by exceeding the corresponding instability threshold. The boundary conditions imposed on the chamber walls (e.g., pinning at the entrance of the waste channel) represent another degree of freedom for microfluidic design: not only do they significantly influence the threshold, but they may also constraint the interface perturbation and guide the destabilized fluid in a preferred direction (here, towards the storage chamber rather than back into the inlet well). In conclusion, reorienting microfluidic chips in a centrifugal force field offers an efficient, low-cost, and reconfigurable control strategy for microfluidic flows. The relevant control parameters, identified in this work, pave the way to the design of microfluidic workflows of arbitrary complexity. This approach will likely meet the needs of miniaturization of sample preparation workflows, especially in R&D environments where robustness and versatility are key.

Acknowledgements

The authors would like to express their gratitude to Olivier Verlaine

for his help with the interface of the centrifugal bench, Denis Vandormael and Stéphane Louis (Sirris) for the manufacturing of microfluidic chips, and Christopher Kune for insightful discussions on the applications of this work. The authors also acknowledge the Walloon Public Service (SPW) for funding the work of this project through the Win2Wal grant 2010126 (ChipOmics).

Appendix A. Model of the instability threshold

The suggested dependence of the acceleration threshold on the chamber dimensions can be rationalized thanks to an energy analysis. The instability threshold should correspond to the smallest acceleration for which some perturbation would decrease the total energy associated with the position of the liquid interface (i.e., this energy would switch from a minimum to a maximum, at least with respect to some perturbations).

Nevertheless, calculating the equilibrium shape of the interface and its stability is still a challenge both in physical and mathematical terms. Among others, properly modeling the contact angle hysteresis induced by a rough and chemically heterogeneous solid surface is far from trivial. Hysteresis would imply that there might be a large number of local minima in the energy landscape. The observed interface shape would then depend on the history, namely, on the conditions in which the liquid was initially loaded in the chamber. In this appendix, for the sake of simplicity, we will assume that the chip/tape surfaces are ideal (i.e., rigid, perfectly smooth, flat, and chemically homogeneous) and with negligible contact angle hysteresis. Nevertheless, any dependence on contact angle highlighted in this simplified analysis should be understood as "unknown and non-trivial dependence on wetting properties, including contact angle hysteresis".

Figure A.10 schematically illustrates a cross-sectional view of the equilibrium shape and perturbations of the interface, for the metering chamber. The equilibrium shape of the interface is described by a function $z = f(x, y)$, where $x \in [0, W]$ and $y \in [0, H]$. Both x, y and z are lengths.

The surface energy of the liquid-air interface is

$$E_{\mathrm{L}} = \gamma_{\mathrm{LG}} \int_0^H \int_0^W \sqrt{1 + (\partial_x f)^2 + (\partial_y f)^2} \mathrm{d}x \mathrm{d}y, \tag{A.1}$$

where γ_{LG} is the liquid surface tension, namely the energy per unit area of this interface. The surface energy associated with the wetting of chamber walls (i.e., the local conversion of a solid/gas interface into a solid/liquid interface) is given by

$$\begin{aligned} E_{\mathrm{S}} &= (\gamma_{\mathrm{SL},1} - \gamma_{\mathrm{SG},1}) \int_0^H f(0, y) \mathrm{d}y + (\gamma_{\mathrm{SL},2} - \gamma_{\mathrm{SG},2}) \int_0^W f(x, H) \mathrm{d}x \\ &+ (\gamma_{\mathrm{SL},3} - \gamma_{\mathrm{SG},3}) \int_0^H f(W, y) \mathrm{d}y + (\gamma_{\mathrm{SL},4} - \gamma_{\mathrm{SG},4}) \int_0^W f(x, 0) \mathrm{d}x, \end{aligned} \tag{A.2}$$

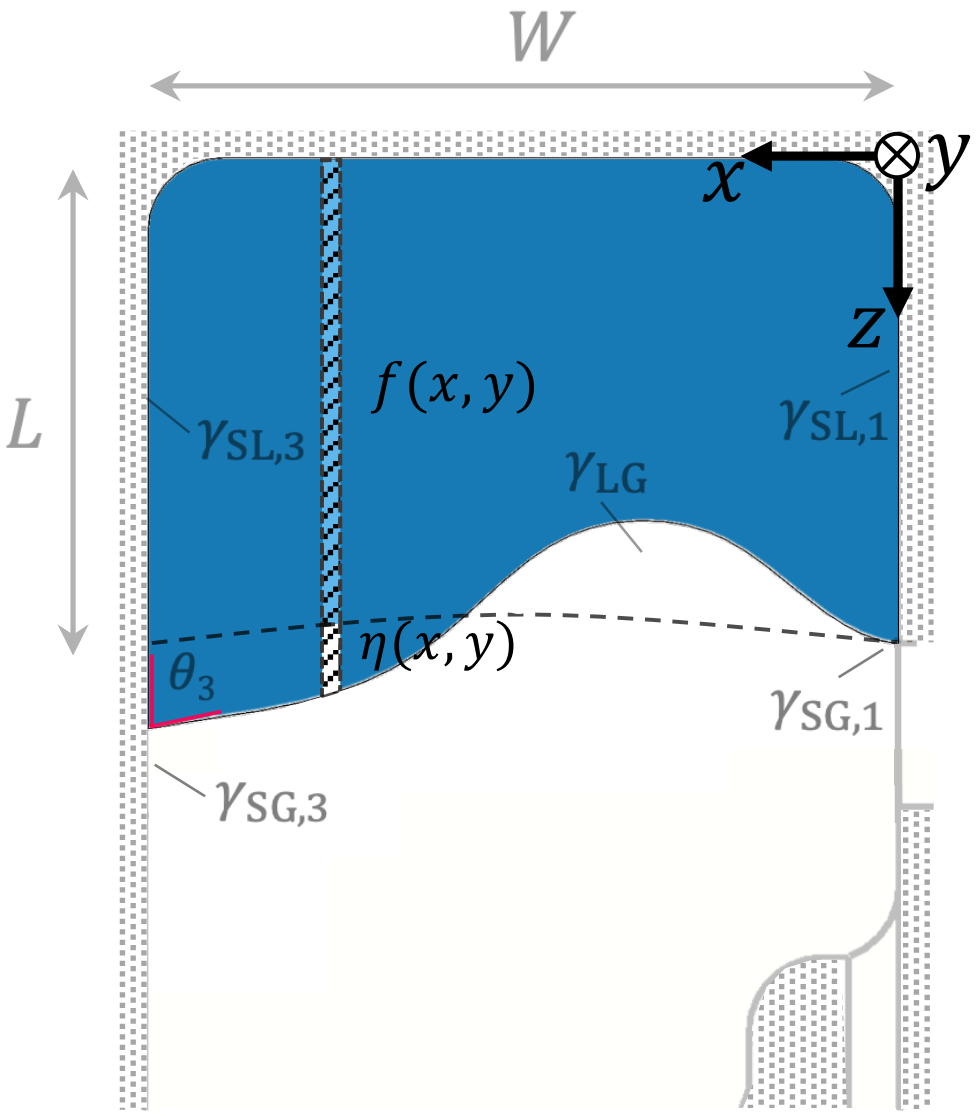

Figure A.10: Schematic cross-sectional view of the equilibrium shape $f(x, y)$ and perturbation $\eta(x, y)$ of the liquid interface in a metering chamber. The interface can be subjected to different boundary conditions on each side: for example, the drawing illustrates a constant contact angle on the left wall (θ_3) at $x = W$, and a pinned contact line on the right wall at the entrance of the waste channel at $x = 0$ (i.e., $\eta(0, y) = 0$). Here, γ_{LG} represents the liquid surface tension, and γ_{SG_i} (resp. γ_{SL_i}) denotes the energy per unit area of the solid/gas (resp. solid /liquid) interface on each wall i.

where $\gamma_{\mathrm{SL},i}$ (resp. $\gamma_{\mathrm{SG},i}$) represents the energy per unit area of solid/liquid (resp. solid/gas) interface on each wall i.
The potential energy associated with centrifugal acceleration is

$$E_a = -\frac{\rho a}{2}\int_0^H \int_0^W f^2 \mathrm{d}x\mathrm{d}y. \tag{A.3}$$

When the interfaces are in stable equilibrium, the total energy $E_\mathrm{L} + E_\mathrm{S} + E_a$ should be minimized. Therefore, we aim at identifying the function $f(x, y)$ that minimizes the functional

$$\begin{aligned} F\left[f(x,y)\right] &= E_\mathrm{L} + E_\mathrm{S} + E_a \qquad (A.4)\\ &= \gamma_\mathrm{LG}\int_0^H\int_0^W \sqrt{1+(\partial_x f)^2+(\partial_y f)^2}\mathrm{d}x\mathrm{d}y - \frac{\rho a}{2}\int_0^H\int_0^W f^2\mathrm{d}x\mathrm{d}y\\ &+ (\gamma_{\mathrm{SL},1}-\gamma_{\mathrm{SG},1})\int_0^H f(0,y)\mathrm{d}y + (\gamma_{\mathrm{SL},2}-\gamma_{\mathrm{SG},2})\int_0^W f(x,H)\mathrm{d}x\\ &+ (\gamma_{\mathrm{SL},3}-\gamma_{\mathrm{SG},3})\int_0^H f(W,y)\mathrm{d}y + (\gamma_{\mathrm{SL},4}-\gamma_{\mathrm{SG},4})\int_0^W f(x,0)\mathrm{d}x. \end{aligned}$$

We consider an infinitesimal perturbation $\eta(x, y)$ of the equilibrium $f(x, y)$ that also satisfies volume conservation, namely

$$\int_0^H\int_0^W \eta \mathrm{d}x\mathrm{d}y = 0. \tag{A.5}$$

We then calculate the resulting modification of F through a Taylor series for $|\eta| \ll 1$:

$$F\left[f+\eta\right] \simeq F[f] + A + \frac{B}{2} + \mathcal{O}(\eta^3) \tag{A.6}$$

with

$$\begin{aligned} A &= \gamma_\mathrm{LG}\int_0^H\int_0^W \frac{\partial_x f\partial_x\eta + \partial_y f\partial_y\eta}{N}\mathrm{d}x\mathrm{d}y - \rho a\int_0^H\int_0^W f\eta\mathrm{d}x\mathrm{d}y\\ &+ (\gamma_{\mathrm{SL},1}-\gamma_{\mathrm{SG},1})\int_0^H \eta(0,y)\mathrm{d}y + (\gamma_{\mathrm{SL},2}-\gamma_{\mathrm{SG},2})\int_0^W \eta(x,H)\mathrm{d}x\\ &+ (\gamma_{\mathrm{SL},3}-\gamma_{\mathrm{SG},3})\int_0^H \eta(W,y)\mathrm{d}y + (\gamma_{\mathrm{SL},4}-\gamma_{\mathrm{SG},4})\int_0^W \eta(x,0)\mathrm{d}x \end{aligned}$$

$$
\begin{aligned}
B &= \gamma_{\mathrm{LG}} \int_0^H \int_0^W \left[\frac{[1+(\partial_y f)^2](\partial_x \eta)^2 - 2\partial_x f \partial_y f \partial_x \eta \partial_y \eta + [1+(\partial_x f)^2](\partial_y \eta)^2}{N^3} \right] \mathrm{d}x\mathrm{d}y \\
&- \rho a \int_0^W \int_0^H \eta^2 \mathrm{d}x\mathrm{d}y, \qquad \text{(A.7)}
\end{aligned}
$$

and where $N = \sqrt{1+(\partial_x f)^2 + (\partial_y f)^2}$. The terms A and B represent the first-order and second-order terms in the perturbation η, respectively. The interface shape f is an equilibrium solution if the corresponding energy F is extremum, which corresponds to $A = 0$. Integration of the first integral of A by parts yields

$$
\begin{aligned}
A &= -\gamma_{\mathrm{LG}} \int_0^H \int_0^W \left[\partial_x \left(\frac{\partial_x f}{N} \right) + \partial_y \left(\frac{\partial_y f}{N} \right) + \frac{\rho a}{\gamma_{\mathrm{LG}}} f \right] \eta \mathrm{d}x\mathrm{d}y \qquad \text{(A.8)} \\
&- \gamma_{\mathrm{LG}} \int_0^H \left[\left(\frac{\partial_x f}{N} - \frac{\gamma_{\mathrm{SL},1} - \gamma_{\mathrm{SG},1}}{\gamma_{\mathrm{LG}}} \right) \eta \right]_{x=0} \mathrm{d}y + \gamma_{\mathrm{LG}} \int_0^W \left[\left(\frac{\partial_y f}{N} + \frac{\gamma_{\mathrm{SL},2} - \gamma_{\mathrm{SG},2}}{\gamma_{\mathrm{LG}}} \right) \eta \right]_{y=H} \mathrm{d}x \\
&+ \gamma_{\mathrm{LG}} \int_0^H \left[\left(\frac{\partial_x f}{N} + \frac{\gamma_{\mathrm{SL},3} - \gamma_{\mathrm{SG},3}}{\gamma_{\mathrm{LG}}} \right) \eta \right]_{x=W} \mathrm{d}y - \gamma_{\mathrm{LG}} \int_0^W \left[\left(\frac{\partial_y f}{N} - \frac{\gamma_{\mathrm{SL},4} - \gamma_{\mathrm{SG},4}}{\gamma_{\mathrm{LG}}} \right) \eta \right]_{y=0} \mathrm{d}x.
\end{aligned}
$$

In this equation, the first integral represents the sole term associated with the shape of the liquid interface across the whole domain under any perturbation η. Consequently, when $A = 0$, the first integral must also be zero; and by taking the volume conservation constraint (A.5) into account, it can then be proven that the expression inside the bracket must be constant. This yields a partial differential equation reminiscent of the Young-Laplace equation

$$
\gamma_{\mathrm{LG}} \left[\partial_x \left(\frac{\partial_x f}{N} \right) + \partial_y \left(\frac{\partial_y f}{N} \right) + \frac{\rho a}{\gamma_{\mathrm{LG}}} f \right] = \mathrm{P}, \qquad \text{(A.9)}
$$

where P is a constant with the dimension of pressure. For any perturbation η, each subsequent integral in Eq. (A.8) independently represents the condition of contact lines on each wall. Therefore, when $A = 0$, the integrand of each integral must be equal to zero, corresponding to the boundary conditions at the walls:

$$
\begin{aligned}
\left[\left(\frac{\partial_x f}{N} - \frac{\gamma_{\mathrm{SL},1} - \gamma_{\mathrm{SG},1}}{\gamma_{\mathrm{LG}}} \right) \eta \right]_{x=0} &= 0, \\
\left[\left(\frac{\partial_y f}{N} + \frac{\gamma_{\mathrm{SL},2} - \gamma_{\mathrm{SG},2}}{\gamma_{\mathrm{LG}}} \right) \eta \right]_{y=H} &= 0,
\end{aligned}
$$

$$\left[\left(\frac{\partial_x f}{N}+\frac{\gamma_{\mathrm{SL},3}-\gamma_{\mathrm{SG},3}}{\gamma_{\mathrm{LG}}}\right)\eta\right]_{x=W} = 0,$$
$$\left[\left(\frac{\partial_y f}{N}-\frac{\gamma_{\mathrm{SL},4}-\gamma_{\mathrm{SG},4}}{\gamma_{\mathrm{LG}}}\right)\eta\right]_{y=0} = 0. \qquad \text{(A.10)}$$

In the first of these four constraints, $[\partial_x f/N]_{x=0}$ is mathematically equivalent to $-\cos\theta_1$, where θ_1 is the angle made by the liquid/gas interface with wall 1 at $x=0$. Therefore, the constraint can be rewritten

$$\left[\left(-\cos\theta_1-\frac{\gamma_{\mathrm{SL},1}-\gamma_{\mathrm{SG},1}}{\gamma_{\mathrm{LG}}}\right)\eta\right]_{x=0}=0. \qquad \text{(A.11)}$$

It is satisfied either when the contact line is pinned ($\eta=0$), or when the contact angle satisfies the Young-Dupré relation ($\cos\theta_1=(\gamma_{\mathrm{SG},1}-\gamma_{\mathrm{SL},1})/\gamma_{\mathrm{LG}}$). A similar reasoning can be done for the three other constraints. In the special case where $|\partial_x f|\ll 1$ and $|\partial_y f|\ll 1$, equation (A.9) resumes to a Poisson's equation for which analytical solutions exist. By contrast, there is no known analytical solution to equations (A.9) and (A.10) in the general case where slopes $\partial_x f$ and $\partial_y f$ are finite, so numerical solutions should be sought (43). Through the boundary conditions (A.10), this solution $f(x,y)$ will necessarily depend on the contact angle (and by extension, contact angle hysteresis) on each wall where the contact line is not pinned.

The second-ordered term $B(f,\eta)$ indicates the stability of the equilibrium solution. Indeed, F is minimized with respect to f when B is strictly positive for any perturbation η. We express the derivatives of η in B in terms of normalized coordinates $\tilde{x}=x/W\in[0,1]$ and $\tilde{y}=y/H\in[0,1]$, namely $\partial_x\eta=(\partial_{\tilde{x}}\eta)/W$ and $\partial_y\eta=(\partial_{\tilde{y}}\eta)/H$:

$$\begin{aligned} B &= \frac{\gamma_{\mathrm{LG}}H}{W}\int_0^1\int_0^1\frac{1+(\partial_y f)^2}{N^3}(\partial_{\tilde{x}}\eta)^2\mathrm{d}\tilde{x}\mathrm{d}\tilde{y}+\gamma_{\mathrm{LG}}\int_0^1\int_0^1\frac{-2\partial_x f\partial_y f}{N^3}(\partial_{\tilde{x}}\eta)(\partial_{\tilde{y}}\eta)\mathrm{d}\tilde{x}\mathrm{d}\tilde{y} \\ &+ \frac{\gamma_{\mathrm{LG}}W}{H}\int_0^1\int_0^1\frac{1+(\partial_x f)^2}{N^3}(\partial_{\tilde{y}}\eta)^2\mathrm{d}\tilde{x}\mathrm{d}\tilde{y}-\rho aWH\int_0^1\int_0^1\eta^2\mathrm{d}\tilde{x}\mathrm{d}\tilde{y}. \qquad \text{(A.12)}\end{aligned}$$

We define

$$\begin{aligned}\chi &= \int_0^1\int_0^1\eta^2\mathrm{d}\tilde{x}\mathrm{d}\tilde{y},\\ c_1 &= \frac{1}{\chi}\int_0^1\int_0^1\frac{1+(\partial_y f)^2}{N^3}(\partial_{\tilde{x}}\eta)^2\mathrm{d}\tilde{x}\mathrm{d}\tilde{y},\end{aligned}$$

$$
\begin{aligned}
c_2 &= \frac{1}{\chi}\int_0^1\int_0^1 \frac{-2\partial_x f\partial_y f}{N^3}(\partial_{\tilde{x}}\eta)(\partial_{\tilde{y}}\eta)\mathrm{d}\tilde{x}\mathrm{d}\tilde{y},\\
c_3 &= \frac{1}{\chi}\int_0^1\int_0^1 \frac{1+(\partial_x f)^2}{N^3}(\partial_{\tilde{y}}\eta)^2\mathrm{d}\tilde{x}\mathrm{d}\tilde{y}.
\end{aligned}
\tag{A.13}
$$

Therefore, by substituting A.13 into A.12,

$$
B = \left[\gamma_{\mathrm{LG}}\left(\frac{c_1}{W^2}+\frac{c_2}{WH}+\frac{c_3}{H^2}\right)-\rho a\right]WH\chi.
$$

Since mathematically $\chi > 0$ for any η, the stability condition $B > 0$ yields

$$
a < a_{\mathrm{c}} = \frac{\gamma_{\mathrm{LG}}}{\rho}\left(\frac{c_1}{W^2}\right)+\frac{\gamma_{\mathrm{LG}}}{\rho}\left(\frac{c_2}{WH}\right)+\frac{\gamma_{\mathrm{LG}}}{\rho}\left(\frac{c_3}{H^2}\right). \tag{A.14}
$$

The coefficients c_1, c_2 and c_3 explicitly depend on the slopes $\partial_x f$ and $\partial_y f$ of the liquid-gas interface. Consequently, they must depend on contact angles (and hysteresis) at each wall, as well as on dimensions W and H. These dependencies cannot be unveiled without explicitly calculating $f(x, y)$, which is out of the scope of this study for the aforementioned reasons. Nevertheless, in the case of contact angles at 90°, $\partial_x f$ and $\partial_y f$ would be equal to zero, and the coefficients c_i would be independent of W and H. By continuity, the dependence of these coefficients on W and H should remain weak for the slightly hydrophilic surfaces considered in this work ($\theta_i \lesssim 90°$). Moreover, we can hint at the variations of c_1 and c_3 with contact angles thanks to the following trick. We consider for example a non-pinned contact line 2 at $y = H$ (i.e., with local contact angle θ_2). We further assume, for the sake of simplicity, that the contact line is almost at constant elevation f, namely

$$
|\partial_x f| \ll |\partial_y f| \tag{A.15}
$$

at $y = H$. Close to this contact line, we mathematically obtain $\partial_y f \simeq \cot\theta_2$, $N \simeq \sqrt{1+(\partial_y f)^2}$, and ultimately $[1+(\partial_y f)^2]/N^3 \simeq \sin\theta_2$. With similar hypotheses, close to contact line 4 at $y = 0$, $[1+(\partial_y f)^2]/N^3 \simeq \sin\theta_4$, and close to the contact line 1 at $x = 0$ (resp. 3 at $x = W$), $[1+(\partial_x f)^2]/N^3 \simeq \sin\theta_1$ (resp. $\sin\theta_3$). Therefore, as long as the solid walls are hydrophilic ($\theta_i < 90°$), decreasing θ_i would yield a decrease of $\sin\theta_i$, and thus a decrease of the contribution of the interface close to the contact lines to the integrals of c_1 and c_3 in Eq.(A.13). In summary, in the first approximation, the coefficients c_i may be considered independent of chip dimensions W and H and dependent on contact angles (and more generally on wetting properties). They are expected to decrease with decreasing contact angles in the case of hydrophilic walls.

References

[1] Vadim Demichev, Lukasz Szyrwiel, Fengchao Yu, Guo Ci Teo, George Rosenberger, Agathe Niewienda, Daniela Ludwig, Jens Decker, Stephanie Kaspar-Schoenefeld, Kathryn S Lilley, et al. dia-pasef data analysis using fragpipe and dia-nn for deep proteomics of low sample amounts. *Nature communications*, 13(1):3944, 2022.

[2] Andreas-David Brunner, Marvin Thielert, Catherine Vasilopoulou, Constantin Ammar, Fabian Coscia, Andreas Mund, Ole B Hoerning, Nicolai Bache, Amalia Apalategui, Markus Lubeck, et al. Ultra-high sensitivity mass spectrometry quantifies single-cell proteome changes upon perturbation. *Molecular systems biology*, 18(3):e10798, 2022.

[3] Andreas Mund, Fabian Coscia, András Kriston, Réka Hollandi, Ferenc Kovács, Andreas-David Brunner, Ede Migh, Lisa Schweizer, Alberto Santos, Michael Bzorek, et al. Deep visual proteomics defines single-cell identity and heterogeneity. *Nature Biotechnology*, 40(8):1231–1240, 2022.

[4] Maowei Dou, Geremy Clair, Chia-Feng Tsai, Kerui Xu, William B Chrisler, Ryan L Sontag, Rui Zhao, Ronald J Moore, Tao Liu, Ljiljana Pasa-Tolic, et al. High-throughput single cell proteomics enabled by multiplex isobaric labeling in a nanodroplet sample preparation platform. *Analytical chemistry*, 91(20):13119–13127, 2019.

[5] Chia-Feng Tsai, Pengfei Zhang, David Scholten, Kendall Martin, Yi-Ting Wang, Rui Zhao, William B Chrisler, Dhwani B Patel, Maowei Dou, Yuzhi Jia, et al. Surfactant-assisted one-pot sample preparation for label-free single-cell proteomics. *Communications Biology*, 4(1):265, 2021.

[6] Robert Gorkin, Jiwoon Park, Jonathan Siegrist, Mary Amasia, Beom Seok Lee, Jong-Myeon Park, Jintae Kim, Hanshin Kim, Marc Madou, and Yoon-Kyoung Cho. Centrifugal microfluidics for biomedical applications. *Lab Chip*, 10(14):1758–1773, 2010.

[7] Oliver Strohmeier, Mark Keller, Frank Schwemmer, Steffen Zehnle, Daniel Mark, Felix von Stetten, Roland Zengerle, and Nils Paust. Centrifugal microfluidic platforms: advanced unit operations and applications. *Chemical Society Reviews*, 44(17):6187–6229, 2015.

[8] Vijaya Sunkara, Sumit Kumar, Jonathan Sabaté Del Río, Insu Kim, and Yoon-Kyoung Cho. Lab-on-a-disc for point-of-care infection diagnostics. *Accounts of chemical research*, 54(19):3643–3655, 2021.

[9] Marc Madou, Jim Zoval, Guangyao Jia, Horacio Kido, Jitae Kim, and Nahui Kim. Lab on a cd. *Annu. Rev. Biomed. Eng.*, 8:601–628, 2006.

[10] Yujin Xiao, Shunji Li, Zheng Pang, Chao Wan, Lina Li, Huijuan Yuan, Xianzhe Hong, Wei Du, Xiaojun Feng, Yiwei Li, et al. Multi-reagents dispensing centrifugal microfluidics for point-of-care testing. *Biosens. Bioelectron.*, 206:114130, 2022.

[11] Tae-Hyeong Kim, Juhee Park, Chi-Ju Kim, and Yoon-Kyoung Cho. Fully integrated lab-on-a-disc for nucleic acid analysis of food-borne pathogens. *Analytical chemistry*, 86(8):3841–3848, 2014.

[12] Daniel Mark, Patrick Weber, Sascha Lutz, Maximilian Focke, Roland Zengerle, and Felix von Stetten. Aliquoting on the centrifugal microfluidic platform based on centrifugo-pneumatic valves. *Microfluid. Nanofluid.*, 10:1279–1288, 2011.

[13] Oliver Strohmeier, Silke Laßmann, Bianca Riedel, Daniel Mark, Günter Roth, Martin Werner, Roland Zengerle, and Felix von Stetten. Multiplex genotyping of kras point mutations in tumor cell dna by allele-specific real-time pcr on a centrifugal microfluidic disk segment. *Microchimica Acta*, 181:1681–1688, 2014.

[14] Jerry M Chen, Po-Chun Huang, and Mou-Gee Lin. Analysis and experiment of capillary valves for microfluidics on a rotating disk. *Microfluidics and Nanofluidics*, 4:427–437, 2008.

[15] Jens Ducrée. Efficient development of integrated lab-on-a-chip systems featuring operational robustness and manufacturability. *Micromachines*, 10(12):886, 2019.

[16] Jens Ducrée, Stefan Haeberle, Sascha Lutz, Sarah Pausch, Felix Von Stetten, and Roland Zengerle. The centrifugal microfluidic bio-disk platform. *J. Micromech. Microeng.*, 17(7):S103, 2007.

[17] Jonathan Siegrist, Robert Gorkin, Liviu Clime, Emmanuel Roy, Régis Peytavi, Horacio Kido, Michel Bergeron, Teodor Veres, and Marc

Madou. Serial siphon valving for centrifugal microfluidic platforms. *Microfluid. Nanofluid.*, 9:55–63, 2010.

[18] Chih Hsin Shih, Hou Jin Wu, and Wen Hao Chen. Robust sequential flow controls on the centrifugal platform. *Adv. Mat. Res*, 254:159–162, 2011.

[19] Per Andersson, Gerald Jesson, Gunnar Kylberg, Gunnar Ekstrand, and Gunnar Thorsén. Parallel nanoliter microfluidic analysis system. *Analytical chemistry*, 79(11):4022–4030, 2007.

[20] Snehan Peshin, Marc Madou, and Lawrence Kulinsky. Microvalves for applications in centrifugal microfluidics. *Sensors*, 22(22):8955, 2022.

[21] David J Kinahan, Sinéad M Kearney, Nikolay Dimov, Macdara T Glynn, and Jens Ducrée. Event-triggered logical flow control for comprehensive process integration of multi-step assays on centrifugal microfluidic platforms. *Lab Chip*, 14(13):2249–2258, 2014.

[22] Ziliang Cai, Jiwen Xiang, Binzhen Zhang, and Wanjun Wang. A magnetically actuated valve for centrifugal microfluidic applications. *Sens. Actuators B-Chem.*, 206:22–29, 2015.

[23] Jong-Myeon Park, Yoon-Kyoung Cho, Beom-Seok Lee, Jeong-Gun Lee, and Christopher Ko. Multifunctional microvalves control by optical illumination on nanoheaters and its application in centrifugal microfluidic devices. *Lab Chip*, 7(5):557–564, 2007.

[24] Ling X Kong, Kshama Parate, Kameel Abi-Samra, and Marc Madou. Multifunctional wax valves for liquid handling and incubation on a microfluidic cd. *Microfluid. Nanofluid.*, 18:1031–1037, 2015.

[25] Chunsun Zhang, Da Xing, and Yuyuan Li. Micropumps, microvalves, and micromixers within pcr microfluidic chips: Advances and trends. *Biotechnol. Adv.*, 25(5):483–514, 2007.

[26] Ziliang Cai, Jiwen Xiang, Hualing Chen, and Wanjun Wang. Membrane-based valves and inward-pumping system for centrifugal microfluidic platforms. *Sensors and Actuators B: Chemical*, 228:251–258, 2016.

[27] Éadaoin Carthy, Brian Hughes, Eimear Higgins, Phil Early, Cian Merne, Darren Walsh, Anne Parle-McDermott, and David J Kinahan. Automated solid phase dna extraction on a lab-on-a-disc with two-degrees of freedom instrumentation. *Analytica Chimica Acta*, 1280:341859, 2023.

[28] Amin Dehghan, Ali Gholizadeh, Mahdi Navidbakhsh, Hossein Sadeghi, and Esmail Pishbin. Integrated microfluidic system for efficient dna extraction using on-disk magnetic stirrer micromixer. *Sens. Actuators B-Chem.*, 351:130919, 2022.

[29] Joo Chuan Yeo, Zhiping Wang, and Chwee Teck Lim. Microfluidic size separation of cells and particles using a swinging bucket centrifuge. *Biomicrofluidics*, 9(5), 2015.

[30] A Kloke, AR Fiebach, S Zhang, L Drechsel, S Niekrawietz, MM Hoehl, R Kneusel, K Panthel, J Steigert, F Von Stetten, et al. The labtube–a novel microfluidic platform for assay automation in laboratory centrifuges. *Lab Chip*, 14(9):1527–1537, 2014.

[31] Tzer Hwai Gilbert Thio, Fatimah Ibrahim, Wisam Al-Faqheri, Jacob Moebius, Noor Sakinah Khalid, Norhayati Soin, Maria Kahar Bador Abdul Kahar, and Marc Madou. Push pull microfluidics on a multi-level 3d cd. *Lab on a Chip*, 13(16):3199–3209, 2013.

[32] Steffen Zehnle, Frank Schwemmer, Günter Roth, Felix von Stetten, Roland Zengerle, and Nils Paust. Centrifugo-dynamic inward pumping of liquids on a centrifugal microfluidic platform. *Lab on a Chip*, 12(24):5142–5145, 2012.

[33] Zahra Noroozi, Horacio Kido, and Marc J Madou. Electrolysis-induced pneumatic pressure for control of liquids in a centrifugal system. *Journal of The Electrochemical Society*, 158(11):P130, 2011.

[34] Guanghui Wang, Ho-Pui Ho, Qiulan Chen, Alice Kar-Lai Yang, Ho-Chin Kwok, Shu-Yuen Wu, Siu-Kai Kong, Yiu-Wa Kwan, and Xuping Zhang. A lab-in-a-droplet bioassay strategy for centrifugal microfluidics with density difference pumping, power to disc and bidirectional flow control. *Lab on a Chip*, 13(18):3698–3706, 2013.

[35] Guanghui Wang, Jie Tan, Minghui Tang, Changbin Zhang, Dongying Zhang, Wenbin Ji, Junhao Chen, Ho-Pui Ho, and Xuping Zhang. Binary

centrifugal microfluidics enabling novel, digital addressable functions for valving and routing. *Lab on a Chip*, 18(8):1197–1206, 2018.

[36] Xiaobao Cao, AJ deMello, and KS Elvira. Enhanced versatility of fluid control in centrifugal microfluidic platforms using two degrees of freedom. *Lab on a Chip*, 16(7):1197–1205, 2016.

[37] Baogang Miao, Niancai Peng, Lei Li, Zheng Li, Fei Hu, Zengming Zhang, and Chaohui Wang. Centrifugal microfluidic system for nucleic acid amplification and detection. *Sensors*, 15(11):27954–27968, 2015.

[38] Matthias Geissler, Liviu Clime, Xuyen D Hoa, Keith J Morton, Harold Hébert, Lucas Poncelet, Maxence Mounier, Mylène Deschênes, Martine E Gauthier, George Huszczynski, et al. Microfluidic integration of a cloth-based hybridization array system (chas) for rapid, colorimetric detection of enterohemorrhagic escherichia coli (ehec) using an articulated, centrifugal platform. *Analytical chemistry*, 87(20):10565–10572, 2015.

[39] Yiqi Chen, Yunzeng Zhu, Minjie Shen, Ying Lu, Jing Cheng, and Youchun Xu. Rapid and automated detection of six contaminants in milk using a centrifugal microfluidic platform with two rotation axes. *Analytical chemistry*, 91(12):7958–7964, 2019.

[40] Lei Li, Baogang Miao, Zheng Li, Zhengming Sun, and Niancai Peng. Sample-to-answer hepatitis b virus dna detection from whole blood on a centrifugal microfluidic platform with double rotation axes. *ACS sensors*, 4(10):2738–2745, 2019.

[41] Yunzeng Zhu, Yiqi Chen, Xiangrui Meng, Jing Wang, Ying Lu, Youchun Xu, and Jing Cheng. Comprehensive study of the flow control strategy in a wirelessly charged centrifugal microfluidic platform with two rotation axes. *Analytical chemistry*, 89(17):9315–9321, 2017.

[42] Gangpei Cai, Yuxin Huang, Bailiang Chen, Yuemin Shen, Xiaolu Shi, Bo Peng, Shengli Mi, and Jiajun Huang. Modular design of centrifugal microfluidic system and its application in nucleic acid screening. *Talanta*, 259:124486, 2023.

[43] Mark M Weislogel and KC Hsieh. Stability of a capillary surface in a rectangular container. In *AIP Conference Proceedings*, volume 420, pages 404–412. American Institute of Physics, 1998.

[44] JW Jacobs and I Catton. Three-dimensional rayleigh-taylor instability part 1. weakly nonlinear theory. *Journal of fluid mechanics*, 187:329–352, 1988.

[45] Pierre-Gilles Gennes, Françoise Brochard-Wyart, David Quéré, et al. *Capillarity and wetting phenomena: drops, bubbles, pearls, waves*. Springer, 2004.

Biography

Ali Gholizadeh has been a research engineer at the University of Liège since 2021. He earned his M.Sc. degree in Mechanical Engineering from Arts et Métiers ParisTech in France in 2020. Before joining ULiège, he gained experience at Fluigent, where he contributed to the development and industrialization of automated microfluidic valves. His current research is at the intersection of chip design, with a focus on (centrifugal) microfluidics and small-scale fluid dynamics, particularly in the context of applications in biology and analytical chemistry.

Tristan Gilet is the head of the Microfluidics Lab (University of Liège). In 2005, he earned two M.Sc. degrees, in Engineering Physics (ULiège) and in Fluid Dynamics (ISAE, Toulouse). He completed a PhD in Physics (ULiège, 2009), then worked as an instructor / post-doctoral fellow at the Department of Mathematics of the Massachusetts Institute of Technology. He is a professor at the University of Liège since 2011. The research of T. Gilet mostly focuses on microscale fluid flows involving capillary forces, including in microfluidic systems and natural environments.

Gabriel Mazzucchelli has been serving as the Scientific Manager of the Mass Spectrometry Lab at the University of Liège since 2008. He obtained his PhD in Biomedical Sciences from ULiège in the same year. Since 2008, he has also held a position as a professor at the University of Liège. His research primarily focuses on single-cell proteomics, downscaled analyses, MALDI imaging in conjunction with laser capture microdissection of tissue sections, followed by shotgun proteomics. Furthermore, he investigates human sweat proteomics in the context of personalized medicine.